Numerical investigation of transient harbor oscillations induced by N-waves

Gao, Junliang
School of Naval Architecture and Ocean Engineering, Jiangsu University of Science and Technology

Ji, Chunyan
School of Naval Architecture and Ocean Engineering, Jiangsu University of Science and Technology

Gaidai, Oleg
School of Naval Architecture and Ocean Engineering, Jiangsu University of Science and Technology

Liu, Yingyi
Research Institute for Applied Mechanics, Kyushu University

他

出版情報：Coastal Engineering. 125, pp.119-131, 2017-04-25. Elsevier
バージョン：

Numerical investigation of transient harbor oscillations induced by N-waves

Junliang Gao [a, b, c, *], Chunyan Ji [a], Oleg Gaidai [a], Yingyi Liu [d], Xiaojian Ma [a]

a School of Naval Architecture and Ocean Engineering, Jiangsu University of Science and Technology, Zhenjiang 212003, China

b Jiangsu Key Laboratory of Coast Ocean Resources Development and Environment Security, Hohai University, Nanjing 210098, China

c State Key Laboratory of Coastal and Offshore Engineering, Dalian University of Technology, Dalian 116024, China

d Research Institute for Applied Mechanics, Kyushu University, Kasuga, Fukuoka 816-8580, Japan

Abstract:

Tsunamis are traveling waves characterized by large amplitudes and long wavelengths close to the coastline. Often, the first couple of leading waves are either leading-elevation N-waves (LEN waves) or leading-depression N-waves (LDN waves). These waves are usually devastating, causing serious damage to coastal infrastructures or even human casualties. Among various natural disasters related to tsunamis, harbor oscillations are one of the most frequent disasters around the world, which can cause excessive movements of moored ships and rupture mooring lines inside the harbor.

In this article, transient harbor oscillations induced by various incident N-waves are first investigated. The transient oscillations are simulated by a fully nonlinear Boussinesq model, FUNWAVE-TVD. The incident N-waves include the TS-type and MS-type isosceles LEN and LDN waves. The TS- and MS-type N-waves correspond to the waveform expressions proposed by Tadepalli and Synolakis [1] and Madsen and Schäffer [2], respectively. This paper focuses on the effects of the incident wave amplitude and its type on the relative wave energy distribution inside the harbor. The maximum runup and rundown of various incident waves are also discussed. For comparison, the transient oscillations excited by solitary waves are also considered. The harbor

*Corresponding author at: School of Naval Architecture and Ocean Engineering, Jiangsu University of Science and Technology, Zhenjiang 212003, China. E-mail address: gaojunliang880917@163.com (J. Gao).

used in this paper is assumed to be long and narrow and has constant depth; the free surface movement inside the harbor is essentially one-dimensional.

This study reveals that, for the given harbor, for the range of the incident wave amplitude and the incident wave types studied in this paper, the larger tsunamis lead to a more uniform relative wave energy distribution inside the harbor. The relative wave energy distributions induced by the LDN waves are always more uniform than those induced by the LEN waves, while the relative wave energy distributions induced by the solitary waves are more concentrated than those induced by the various N-waves. When the incident wave amplitude is relatively large, the maximum runups of the LDN waves are considerably larger than those of the solitary waves, while those of the LEN waves are much less than those of the solitary waves.

Keywords:

Harbor oscillations; Boussinesq wave model; N-waves; Wave energy distribution; Wave runup and rundown

1. Introduction

Long waves may be amplified inside semi-enclosed bodies of water, such as bays or harbors, when the incident wave period coincides with one of the eigenperiods of the semi-enclosed water body. This phenomenon is known as harbor oscillation (resonance), which has caught the attention of many researchers for several decades [3]. Significant harbor oscillations can be induced by a variety of dynamic forcings, including short wave groups, infragravity waves, atmospheric fluctuations, tsunamis and shear flow traveling into bays or harbors [4-14]. By creating unacceptable vessel movements, harbor oscillations may interrupt cargo handling, disturb operational efficiency and generate excessive mooring forcing that may break mooring lines [15, 16].

Among various generation mechanisms, transient harbor oscillations induced by tsunamis are usually destructive. Tsunamis are triggered by submarine earthquakes, undersea volcanic eruptions or offshore landslides. As tsunamis approach the coastal area, the wave height increases significantly due to continuous decreasing of the water depth [17]. For example, the Indian Ocean tsunami, which was induced by the Sumatra earthquake on the December 26, 2004, propagated for

about 2 h to Colombo harbor (Sri Lanka), triggering extreme oscillations with the maximum wave height of 3.87 m and the resonant period of about 75 min. It then propagated for about 14 h to Bunbury harbor (Western Australia), triggering oscillations with the maximum wave height of 1.75 m [12].

Although research efforts on harbor oscillations began in the early 1950s [18], the majority of past studies have been restricted to the stationary oscillations induced by steady wave climate. In response to periodic forcing waves, oscillations within the harbor at their eigenperiods increase significantly in magnitude before the energy input from the external source is balanced by losses owing to frictions, boundary absorption and radiation from the entrance [18-27]. Obviously, most of the characteristics of harbor resonance found in these works are only suitable for the steady wave conditions. While the studies on transient oscillations induced by transient long waves started relatively late and few researchers focused on this problem, overall. Using the theoretical and experimental methods, Lepelletier and Raichlen [28] studied transient nonlinear oscillations inside harbors induced by transient long waves, such as tsunamis. Using laboratory experiments combined with a fully nonlinear Boussinesq model, Dong et al. [9] explored the resonant response of a rectangular harbor with constant depth to subaerial landslide-generated impact waves. By developing a second-order dispersive Boussinesq model that can describe the generation and propagation of earthquake- and landslide-induced tsunamis, Wang et al. [29] systematically investigated the transient oscillations induced by seafloor movements inside a harbor of constant slope. More recently, using a Boussinesq model, Gao et al. [11] and Gao et al. [14] carried out a series of numerical experiments on transient harbor resonance triggered by solitary waves, and systematically studied the relative wave energy distribution inside the harbor.

As some features observed in the tsunami events can be well simulated by solitary waves, for instance, the stable form of hump-like waves after a long period of propagation, lots of analytical, numerical and experimental investigations on solitary waves have been connected to tsunamis for decades (e.g., Liu et al. [30], Camfield and Street [31], Goring [32], Synolakis [33], Hsiao et al. [34], Lo et al. [35]). However, based on several field observations which described that the leading tsunami wave was often preceded by a depression, Tadepalli and Synolakis [1] proposed the concept of N-waves to obtain better geophysical relevancy. Due to more and more evidences from field observations, it has been widely accepted that the leading tsunami wave reaches coastlines

like either leading-depression N-waves (LDN waves) or leading-elevation N-waves (LEN waves). Subsequently, based on the viewpoint that the time and length scales of solitary waves are distinctively different with those of real tsunamis, Madsen and Schäffer [2] also doubted whether the classical solitary wave theory can fully represent main characteristics of real tsunami events in tsunami studies. Tadepalli and Synolakis [1] and Madsen and Schäffer [2] proposed different formulations for N-wave profiles.

So far, studies on transient harbor resonance induced by tsunamis are mostly confined to using solitary waves or cnoidal waves to represent real tsunamis (e. g., Dong et al. [9], Gao et al. [11], Gao et al. [14], Lepelletier and Raichlen [28]). The coastal effects related to N-waves are only restricted to determining their runup and rundown on plane beaches (e. g., Tadepalli and Synolakis [1], Madsen and Schäffer [2], Zhao et al. [17], Charvet et al. [36]). To the best of the authors' knowledge, investigations of transient harbor resonance excited by N-waves have not been reported in the literature. In order to expand the knowledge of tsunami-induced oscillations, this paper uses N-waves to explore related transient oscillation phenomena. The focus of this paper is to comprehensively investigate the relative wave energy distribution inside the harbor during transient oscillations induced by normal-incident N-waves with different amplitudes and different types of initial incident waveforms. It should be emphasized that it is vitally important to accurately predict and systematically investigate the wave energy distribution inside the harbor excited by tsunamis, which can provide important hydrodynamic information for predicting the motion responses of the moored ships inside the harbor [15, 16]. The maximum runup and rundown of the N-wave inside the harbor are also discussed. Effects of different amplitudes and different types of the initial incident N-waves on these phenomena are studied systematically. Meanwhile, to compare similarities and differences between oscillations induced by N-waves and those by solitary waves, the transient oscillations excited by solitary waves are also simulated, which has been investigated by Gao et al. [11] and Gao et al. [14] and is only taken as a control group in this paper. In this paper, all numerical experiments are performed using a fully nonlinear Boussinesq wave model, FUNWAVE-TVD [37]. For simplification, the harbor is assumed to be long and narrow, and has a flat bottom; the free surface movement inside the harbor then essentially becomes one-dimensional.

The remainder of the paper is organized as follows: Section 2 describes the numerical model

and the data analysis technique. The applicability of the former on the transient harbor oscillations is verified by physical experiment. Section 3 presents the incident wave parameters and the setup of the numerical wave tank. Section 4 demonstrates the simulation results, which are explained in detail. Concluding remarks based on the results are given in Section 5.

2. Numerical model and data analysis technique

2.1. Numerical model description

In this section, the fully nonlinear Boussinesq wave model, FUNWAVE-TVD, developed by Shi et al. [37] is briefly introduced. The model solves the fully nonlinear Boussinesq equations of Chen [38] using a hybrid finite volume-finite difference scheme, and incorporates a moving reference level as in Kennedy et al. [39]. The terms in the model are retained to $O(\mu^2)$ in frequency dispersion and to all orders in nonlinearity a/h (where $\mu=h/L$, h denotes the local still water depth, L denotes the wavelength, and a denotes the wave amplitude). The governing equations in FUNWAVE-TVD are organized in a well-balanced conservative form, which are given by

$$\eta_t + \nabla \cdot \mathbf{M} = 0 \tag{1}$$

$$\begin{aligned} &\mathbf{M}_t + \nabla \cdot \left[\frac{\mathbf{MM}}{H}\right] + \nabla\left[\frac{1}{2} g\left(\eta^2 + 2h\eta\right)\right] \\ &= H\left\{\bar{\mathbf{u}}_{2,t} + \mathbf{u}_\alpha \cdot \nabla \bar{\mathbf{u}}_2 + \bar{\mathbf{u}}_2 \cdot \nabla \mathbf{u}_\alpha - \mathbf{V}_1 - \mathbf{V}_2 - \mathbf{V}_3 - \mathbf{R}\right\} + g\eta\nabla h \end{aligned} \tag{2}$$

where g denotes the gravitational acceleration, η denotes the local surface displacement, $H=h+\eta$ denotes the total local water depth, $\nabla = \left((\partial/\partial x),(\partial/\partial y)\right)$ is the horizontal gradient operator. $\mathbf{M}$ is the horizontal volume flux expressed as

$$\mathbf{M} = H\left\{\mathbf{u}_\alpha + \bar{\mathbf{u}}_2\right\} \tag{3}$$

where $\mathbf{u}_\alpha$ denotes the velocity at a reference elevation $z_\alpha = \zeta h + \beta\eta$ with $\zeta = -0.53$ and $\beta = 0.47$, and $\bar{\mathbf{u}}_2$ is the depth-averaged $O(\mu^2)$ contribution to the horizontal velocity field, given by

$$\bar{\mathbf{u}}_2 = \left[\frac{z_\alpha^2}{2} - \frac{1}{6}\left(h^2 - h\eta + \eta^2\right)\right]\nabla B + \left[z_\alpha + \frac{1}{2}\left(h - \eta\right)\right]\nabla A \tag{4}$$

where $A = \nabla \cdot \left(h\mathbf{u}_\alpha\right)$ and $B = \nabla \cdot \mathbf{u}_\alpha$. $\mathbf{V}_1$ and $\mathbf{V}_2$ are terms representing the dispersive Boussinesq terms given by

$$\mathbf{V}_1 = \left\{ \frac{z_\alpha^2}{2} \nabla B + z_\alpha \nabla A \right\}_t - \nabla \left[\frac{\eta^2}{2} B_t + \eta A_t \right] \tag{5}$$

$$\mathbf{V}_2 = \nabla \left\{ (z_\alpha - \eta)(u_\alpha \cdot \nabla) A + \frac{1}{2}(z_\alpha^2 - \eta^2)(u_\alpha \cdot \nabla) B + \frac{1}{2}(A + \eta B)^2 \right\} \tag{6}$$

The term $\mathbf{V}_3$ represents the $O(\mu^2)$ contribution to the vertical vorticity and may be written as

$$\mathbf{V}_3 = \omega_0 \mathbf{i}^z \times \bar{\mathbf{u}}_2 + \omega_2 \mathbf{i}^z \times \mathbf{u}_\alpha \tag{7}$$

where

$$\omega_0 = (\nabla \times \mathbf{u}_\alpha) \cdot \mathbf{i}^z = v_{\alpha,x} - u_{\alpha,y} \tag{8}$$

$$\omega_2 = (\nabla \times \bar{\mathbf{u}}_2) \cdot \mathbf{i}^z = z_{\alpha,x} (A_y + z_\alpha B_y) - z_{\alpha,y} (A_x + z_\alpha B_x) \tag{9}$$

and $\mathbf{i}^2$ is the unit vector in the vertical direction. **R** represents diffusive and dissipative terms including bottom friction and subgrid lateral turbulent mixing.

FUNWAVE-TVD is solved by a high-order shock-capturing TVD (Total Variation Diminishing)-type scheme, which allows the model to be capable of simulating wave breaking and associated wave energy dissipation without relying on empirical formulations [37, 40]. Besides, the moving shoreline is captured by a robust wetting-drying scheme, and a third-order Strong Stability-Preserving Runge–Kutta scheme is adopted for adaptive time stepping. The model is parallelized using the Message Passing Interface (MPI) with non-blocking communication. With these improvements, the model has been shown to be more robust in predicting wave processes in the nearshore, including wave shoaling, refraction, diffraction, breaking as well as wave runup/rundown on the plane and natural beaches [37].

2.2. Numerical model verification by physical experiment

To verify the applicability of the FUNWAVE-TVD model in simulating the transient harbor resonance induced by tsunamis, the model was used to simulate the laboratory experiments of Dong et al. [9]. The experiments were conducted in a wave flume with 50.0 m long and 4.0 m wide. An elongated rectangular harbor was located at the center of the flume. The harbor was 3.0 m in length and 0.3 m in width and had a flat bottom inside. The water depth *h* was constant at 0.3 m everywhere throughout the experiments. Impact waves were generated by two different rigid blocks, a big block (BB) and a small block (SB), dropping vertically from the still-water surface into the left end of the wave flume. For comparison with the experimental results, Dong et al. [9]

used a fully nonlinear Boussinesq model FUNWAVE 2.0 [41] to simulate the response of the same harbor to normal-incident solitary waves propagating from the same flume.

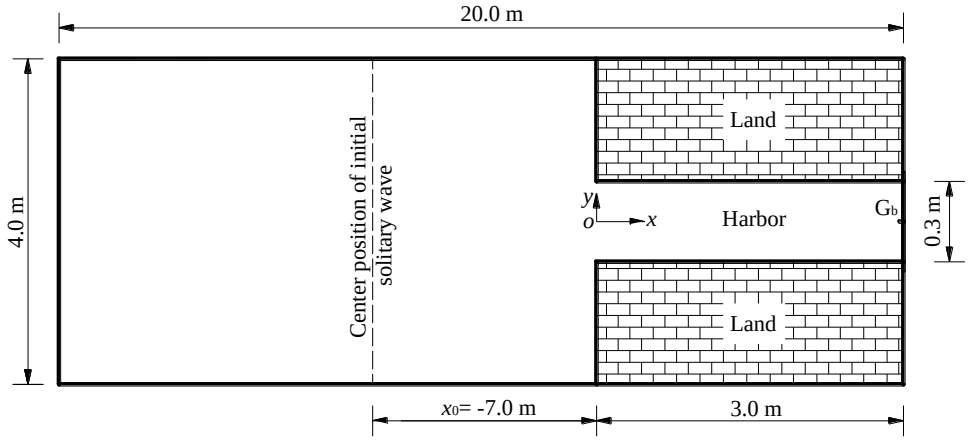

Fig. 1. Sketch of the numerical experimental setup for reproducing the experiments of Dong et al. [9]. Based on its geometrical symmetry with respect to the x-axis, only half of the domain (i.e., $y \geq 0$) is used as the computational domain for simulations.

Fig. 1 shows the sketch of the numerical experimental setup for reproducing the experiments of Dong et al. [9]. The numerical wave flume has a length of 20.0 m and a width of 4.0 m. It should be noted that to reduce the computational cost, only half of the domain (i.e., $y \geq 0$) is used for simulations based on the geometrical symmetry with respect to the x-axis. The grid sizes Δx and Δy are uniform in 0.02 m in the whole domain. All boundaries are set to be fully reflective. The initial incident solitary wave is expressed as

$$\eta(x) = A_0 \mathrm{sech}^2\left[k(x - x_0)\right], k = \sqrt{\frac{3A_0}{4h^3}}, \tag{10}$$

and the initial velocity is taken as a linear expression

$$u(x) = \sqrt{\frac{g}{h}}\eta(x), \tag{11}$$

where g, A_0, and x_0 denote the gravitational acceleration, the wave amplitude and the center position of the initial incident solitary wave, respectively. The amplitude of the initial incident solitary wave ranges from 0.5 cm to 3.0 cm. The center position of the initial incident solitary for all simulations is set to $x_0 = -7.0$ m. One wave gauge G_b is deployed at the backwall of the harbor (x= 3.0 m) to measure the maximum oscillation (runup). The total simulation time is 10.0 s.

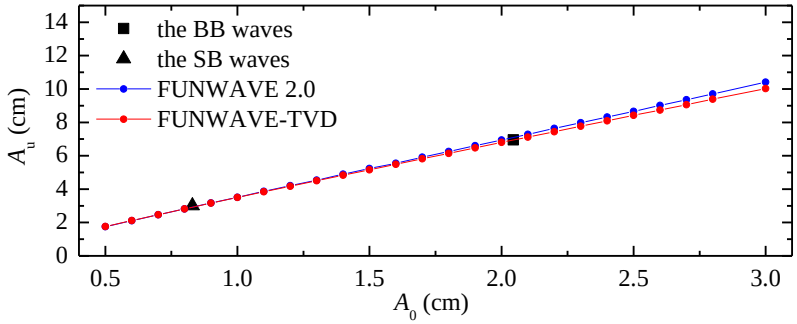

Fig. 2. Variation of the maximum oscillation (runup), A_u, inside the harbor with respect to the incident wave amplitude, A_0

Fig. 2 shows the comparison of the maximum oscillation, A_u, inside the harbor predicted by the FUNWAVE-TVD model with the experimental and numerical data of Dong et al. [9]. It is shown that the numerical results of the FUNWAVE-TVD model agree well with both of the experimental data and the numerical results of the FUNWAVE 2.0 model. When the incident wave amplitude, A_0, is small ($A_0 \leq 1.5$ cm), the predicted maximum oscillation by the FUNWAVE-TVD model is almost identical to that by the FUNWAVE 2.0 model. With the increase of the wave amplitude, the former becomes slightly less than the latter. However, the former seems to give better prediction of the maximum oscillation generated by the BB wave than the latter.

2.3. Data analysis technique

The wave conditions inside the harbor for all numerical experiments are analyzed by the normal mode decomposition (NMD) method. The NMD method was proposed originally by Sobey [42] to calculate the eigenfrequencies, the eigenmodes and the response amplitudes of different modes in natural harbors that are subjected to storm tides or tsunamis. This method consists of two calculating steps. The first step involves the prediction of the discrete set of eigenfrequencies and associated eigenmodes of the semi-enclosed body of water. In the second step, the prediction of the response amplitudes at the discrete resonant modes is formulated and solved as a problem in multi-dimensional optimization, where the eigenfrequencies and eigenmodes calculated in the first step are used as known variables. Recently, the method was improved by Gao et al. [43] to predict the eigenfrequencies and eigenmodes more accurately. Subsequently, by using the NMD method, Gao et al. [11] and Gao et al. [14] systematically analyzed the relative wave energy distribution inside the harbor during transient harbor

oscillations induced by solitary waves. For the theory of the NMD method, the interested reader is referred to Sobey [42] and Gao et al. [43]. Similar to Gao et al. [11] and Gao et al. [14], all numerical experiments in this paper also adopt this method to analyze the relative wave energy distribution inside the harbor induced by different types of incident tsunamis.

3. Numerical experimental setup

3.1. Incident wave parameters

As mentioned in the introduction, Tadepalli and Synolakis [1] first introduced the concept of the N-wave in tsunami studies. In their paper, the N-wave was categorized into the isosceles and the generalized N-wave, based on whether the crest and trough of the N-wave had the equal amplitude. Both of the categories consist of leading-elevation N-waves (LEN waves) and leading-depression N-waves (LDN waves). In the present work, only the isosceles LEN and LDN waves are considered. The isosceles N-wave formulated by Tadepalli and Synolakis [1] is given by

$$\eta(x) = \pm\frac{3\sqrt{3}}{2}A_0\,\mathrm{sech}^2\left(k_0\left(x-x_0\right)\right)\tanh\left(k_0\left(x-x_0\right)\right),\ k_0 = \frac{3}{2h}\sqrt{\frac{A_0}{h}}\sqrt{\frac{3}{4}}. \tag{12}$$

The plus and minus signs correspond to the LEN and LDN waves, respectively.

To compare the transient harbor resonance induced by different types of the incident N-wave, the N-wave formulated by Madsen and Schäffer [2] is also considered. In that paper, the N-wave was constructed by the superposition of two single waves. If the single waves are described with the expressions of positive and negative solitary waves, the isosceles N-wave takes the form:

$$\eta(x) = \pm A_1\left\{\mathrm{sech}^2\left(k_1\left(x-x_0\right)-\frac{\pi}{4}\right)-\mathrm{sech}^2\left(k_1\left(x-x_0\right)+\frac{\pi}{4}\right)\right\},\ k_1 = \sqrt{\frac{3A_1}{4h^3}}. \tag{13}$$

The plus and minus signs here also correspond to the LEN and LDN waves, respectively. It should be noted that the amplitude of the N-wave in Eq. (13) is not equal to A_1. As Madsen and Schäffer [2] have noted, this difference should be taken into consideration if the transient harbor oscillations induced by different types of tsunami waves are to be compared in absolute terms, and A_1 should take a value that ensures the N-wave to have the same amplitude, A_0, as described in Eq. (10) and (12). Madsen and Schäffer [2] also presented the following relationship

$$A_1 = 1.165A_0. \tag{14}$$

It should be stressed that, in Madsen and Schäffer [2], to better match the real tsunamis, the

relationship between the temporal and spatial scales of the wave and the wave amplitude is not confined to the classical solitary wave theory and is allowed to be freely changed. However, to compare the N-wave proposed by Madsen and Schäffer [2] with the N-wave proposed by Tadepalli and Synolakis [1] and the conventional solitary wave directly in an idealized condition, the constrained relationship identical to the classical solitary wave theory is retained in the present work. For ease of description, hereinafter, the N-waves expressed by Eqs. (12) and (13) are referred to as TS- and MS- type isosceles N-waves, respectively.

For all numerical experiments studied in this paper, the water depth at the open ocean is set to a constant, h=10.0 m (this will be described in detail in Section 3.2). Under this condition, Table 1 shows the specific parameters of different types of incident waves for all of the simulations. This paper includes five groups of numerical experiments, namely, Groups A-E. Each of the five groups consists of eight cases with different incident wave amplitudes. The incident wave amplitude, A_0, in each group ranges from 0.005 m to 0.30 m to systematically investigate the effect of the wave amplitude variation on the relative wave energy distribution inside the harbor. In Groups A-D, the different types of N-waves are used as the initial incident waves, that is, the TS-type LEN waves, the TS-type LDN waves, the MS-type LEN waves, and the MS-type LDN waves, respectively. In Group E, the conventional solitary waves are adopted as initial incident waves. It should be noted that the related transient oscillation phenomena induced by solitary waves, including the wave energy distribution and maximum wave runup inside the harbor, has been investigated in Gao et al. [11] and Gao et al. [14]. The purpose of constructing Group E is to understand which features are common and which are different regarding these phenomena excited by N-waves and by solitary waves. L_0, in the table, denotes the wavelength of the incident wave, which will be defined in the next paragraph.

Fig. 3 compares the waveforms of the various types of initial incident waves with A_0=0.10 m. The circle in the figure stands for the wavefront of the corresponding incident wave, which is defined as $\eta_f = \pm 0.05 A_0$, where η_f denotes the free surface elevation of the wavefront. In this paper, we define the wavelength of the incident wave, L_0, as twice the distance between the wavefront and x_0. As expected, for the LEN and LDN waves of both the TS-type and the MS-type, their waveforms are identical except that they are antiphase. For the same wave amplitude, the wavelengths of the solitary waves are larger than those of the TS-type N-waves by approximately

1.32 times and less than those of the MS-type N-waves by approximately 0.78 times (refer to Table 1).

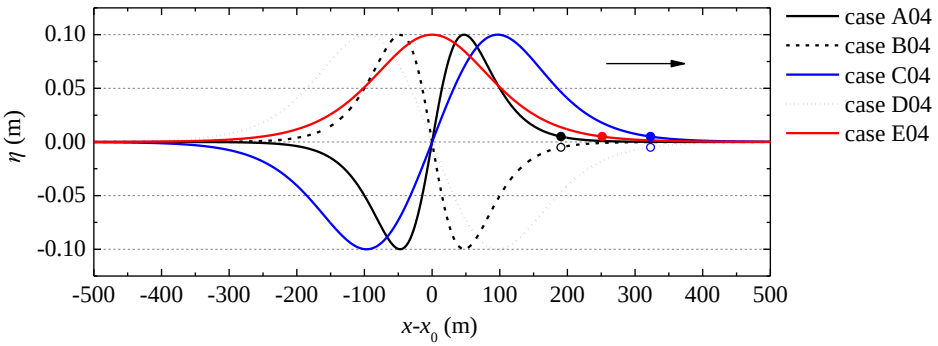

Fig. 3. Waveform comparison of the different initial incident waves with A_0=0.10 m. The circle denotes the wavefront of the corresponding waveform.

300 **Table 1** Wave parameters of initial incident waves in all numerical experiments

Group	Initial incident waveform	Case	A_0 (m)	L_0 (m)
A	TS-type LEN wave	A01	0.005	1703.6
		A02	0.01	1204.6
		A03	0.05	538.8
		A04	0.10	381.0
		A05	0.15	311.0
		A06	0.20	269.4
		A07	0.25	241.0
		A08	0.30	220.0
B	TS-type LDN wave	B01	0.005	1703.6
		B02	0.01	1204.6
		B03	0.05	538.8
		B04	0.10	381.0
		B05	0.15	311.0
		B06	0.20	269.4
		B07	0.25	241.0
		B08	0.30	220.0
C	MS-type LEN wave	C01	0.005	2890.0
		C02	0.01	2042.5
		C03	0.05	913.4
		C04	0.10	645.8
		C05	0.15	527.4
		C06	0.20	456.9
		C07	0.25	408.6
		C08	0.30	372.0
D	MS-type LDN wave	D01	0.005	2890.0
		D02	0.01	2042.5
		D03	0.05	913.4
		D04	0.10	645.8
		D05	0.15	527.4
		D06	0.20	456.9
		D07	0.25	408.6
		D08	0.30	372.0
E	Solitary wave	E01	0.005	2249.7
		E02	0.01	1590.8
		E03	0.05	711.4
		E04	0.10	503.1
		E05	0.15	410.7
		E06	0.20	355.7
		E07	0.25	318.2
		E08	0.30	290.4

301

302

303

3.2. Numerical wave tank

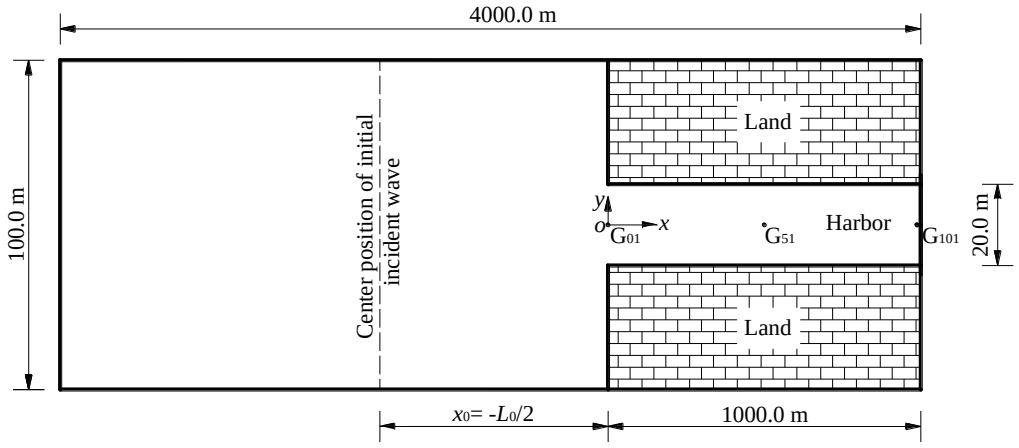

Fig. 4. Sketch of the numerical experimental setup used in the numerical experiments. Based on its geometrical symmetry with respect to the *x*-axis, only half of the domain (i.e., $y \geq 0$) is used as the computational domain for the simulations.

Fig. 4 demonstrates the sketch of the numerical experimental setup used in the numerical experiments. Similar to Dong et al. [9], an elongated rectangular harbor with constant depth is used in the numerical experiments. The harbor has a length of 1000.0 m and a width of 20.0 m. The water depth inside and outside the harbor is set to h=10.0 m. The dimensions of the numerical wave tank are 4000.0 m × 100.0 m. Identical to Fig. 1, based on the geometrical symmetry, only half of the domain (i.e., $y \geq 0$) is used as the computational domain for the simulations. There are 101 wave gauges ($G_{01} - G_{101}$) deployed equidistantly with a spacing of 10.0 m along the center line of the harbor. Gauges G_{01} and G_{101} are those at the entrance and the backwall of the harbor, respectively. The grid sizes Δx and Δy are uniform in 1.0 m throughout the numerical wave tank, and the computational domain (i.e., $y \geq 0$) consists of 204,051 nodes and 200,000 rectangular elements. All of the boundaries are set to be fully reflective. As an initial condition, in each case, the wavefront of the initial incident wave is set at the harbor entrance, i.e., $x_0 = -L_0/2$. The simulation time is 350.0 s for all cases.

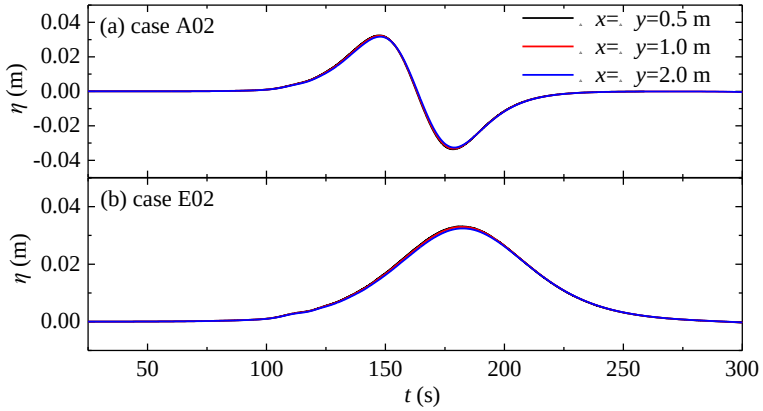

Fig. 5. Time series of the wave elevations at gauge G_{101} for different grid sizes for cases A02 and E02

To verify whether the grid size $\Delta x=\Delta y=1.0$ m is sufficiently fine to obtain convergent simulation results, two other different grid sizes, i.e., $\Delta x=\Delta y=0.5$ m and $\Delta x=\Delta y=2.0$ m, are also used to reproduce the numerical simulations for cases A02 and E02. The size and layout of the numerical wave tank and the initial incident wave condition for the three different grid sizes are set to be identical. Fig. 5 compares the time series of the wave elevations at gauge G_{101} for the three different grid sizes for both of the cases. It can be found that the simulation results obtained by the three different grid sizes are almost identical to each other, which illustrates that the grid size $\Delta x=\Delta y=1.0$ m used in this paper is indeed able to obtain convergent simulation results.

4. Results and discussion

4.1. Calculation process of the response amplitude of the different modes

In all of the numerical experiments, only the wave conditions during the period from t_0 to t_1 are adopted to decompose the response amplitudes of the different resonant modes inside the harbor. t_0 and t_1 denote the moment that the incident wave completely enters the harbor from the open sea and the moment that the reflected wave from the backwall of the harbor begins to propagate out of the harbor, respectively. Take cases A03, B03 and C03 for example. Fig. 6 shows the time series of the wave elevations at gauge G_{01} in these cases. For cases A03 and B03 (see Fig. 6a and b), both the incident LEN and LDN waves have already completely entered the harbor at t_0=65.0 s, and the reflected waves from the backwall begin to propagate out of the harbor at t_1=195.0 s. For case E03, in which the harbor is exposed to a solitary wave (see Fig. 6c), the moments t_0 and t_1 are 90.0 s and 195.0 s, respectively.

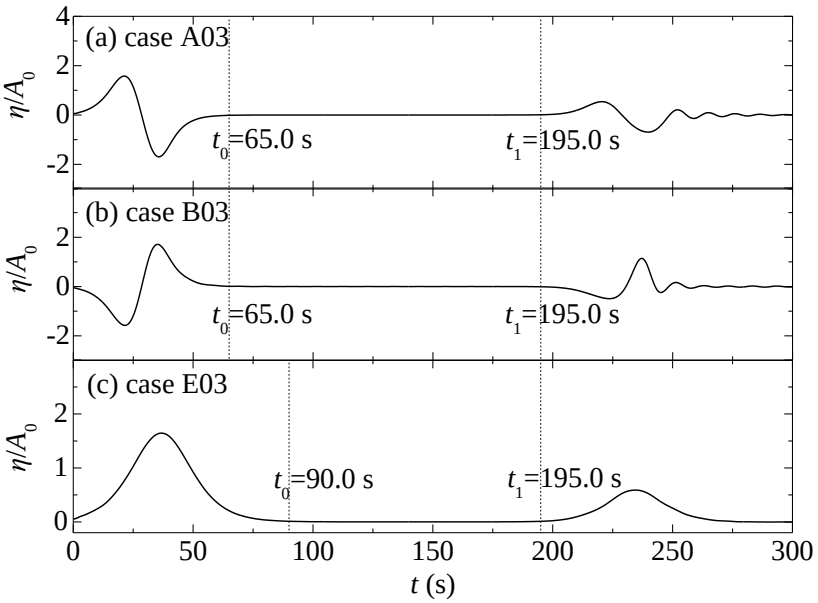

Fig. 6. Time series of the wave elevations at gauge G_{01} for cases A03, B03 and E03

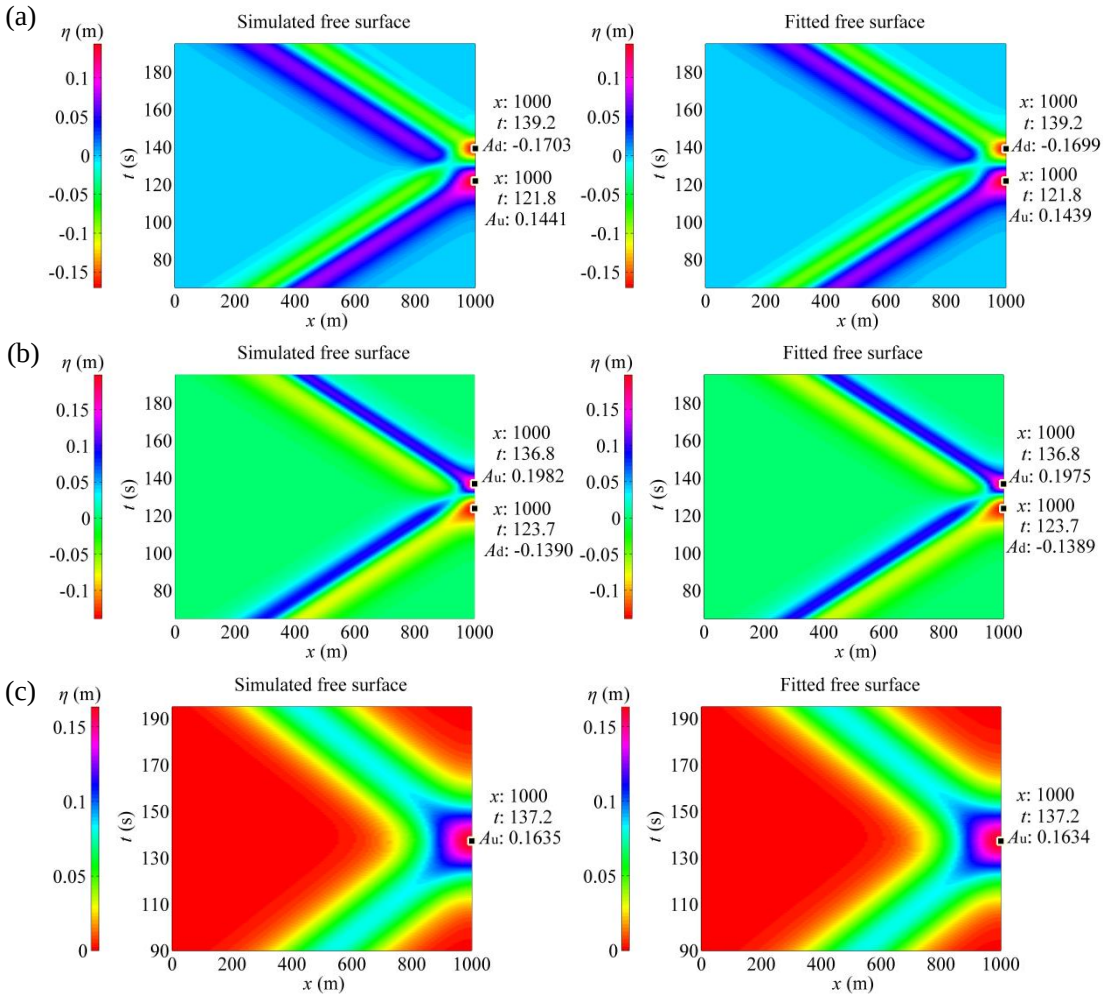

Fig. 7. Comparison of the simulated free surfaces and the corresponding fitted free surfaces for (a) case A03, (b) case B03 and (c) case E03

Fig. 7 compares the simulated free surfaces using the FUNWAVE-TVD model and the corresponding fitted free surfaces using the NMD method in cases A03, B03 and E03. The lowest 40 resonant modes are considered in fitting the free surface. For all three cases, the fitted free surfaces coincide very well with the simulated free surfaces. For case A03 (Fig. 7a), the simulated free surface inside the harbor has a maximum runup of 0.1411 m at x=1000.0 m and t=121.8 s and has a maximum rundown of -0.1703 m at x=1000.0 m and t=139.2 s; at the same position and the same time, the fitted free surface has a maximum runup of 0.1439 m and a maximum rundown of -0.1699 m. For case B03 (Fig. 7b), the simulated free surface inside the harbor has a maximum runup of 0.1982 m at x=1000.0 m and t=136.8 s and has a maximum rundown of -0.1390 m at x=1000.0 m and t=123.7 s; at the same position and the same time, the fitted free surface has a maximum runup of 0.1975 m and a maximum rundown of -0.1389 m. For case E03 (Fig. 7c), the simulated free surface inside the harbor has a maximum runup of 0.1635 m at x=1000.0 m and t=137.2 s, while at the same position and the same time, the fitted free surface has a maximum runup of 0.1634 m. Because of the significance and typicality of the maximum runup/rundown, we define the numerical fitting error (*NFE*) of the NMD method to be the maximum relative error between the maximum values of the simulated and the fitted runup/rundown, that is,

$$NFE=\begin{cases}\left|\left[(A_{\mathrm{u}})_{\mathrm{fitted}}-A_{\mathrm{u}}\right]/A_{\mathrm{u}}\right|\times 100\%, \text{ for the solitary wave}\\ \max\left\{\left|\left[(A_{\mathrm{u}})_{\mathrm{fitted}}-A_{\mathrm{u}}\right]/A_{\mathrm{u}}\right|,\left|\left[(A_{\mathrm{d}})_{\mathrm{fitted}}-A_{\mathrm{d}}\right]/A_{\mathrm{d}}\right|\right\}\times 100\%, \text{ for the N-wave}\end{cases} \tag{15}$$

in which A_{u} and $(A_{\mathrm{u}})_{\mathrm{fitted}}$ denote the simulated and the fitted maximum runups, respectively; A_{d} and $(A_{\mathrm{d}})_{\mathrm{fitted}}$ denote the simulated and the fitted maximum rundowns, respectively. The *NFE* reflects the accuracy of the NMD method in separating the response amplitudes of the different resonant modes. The *NFE*s for cases A03, B03 and E03 are 0.23%, 0.35% and 0.06%, respectively. Fig. 8 shows the *NFE*s in all numerical experiments. It is shown that, in general, the *NFE* in each group increases with the incident wave amplitude, which agrees with the finding in Gao et al. [43]. The *NFE*s in all numerical experiments are less than 5.0%, which guarantees the accurate prediction of the response amplitudes of the different resonant modes in all simulations. The decomposed results of the response amplitude of different modes in all numerical experiments will be demonstrated in Section 4.2.

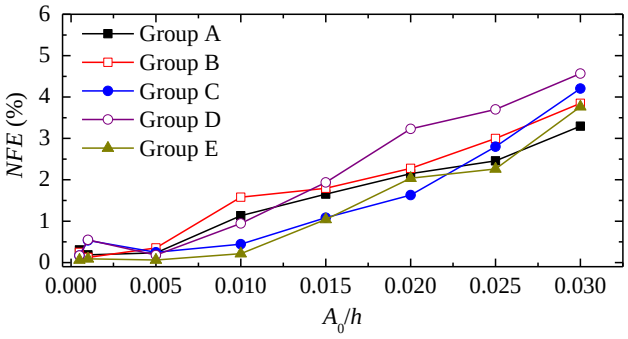

Fig. 8. Numerical fitting errors (*NFE*s) for all cases

4.2. Effect of the incident wave amplitude on the relative wave energy

In this article, the "relative amplitude" in each case is defined as the ratio of the response amplitude of each resonant mode to the incident wave amplitude, that is,

$$\bar{A}_i = \frac{A_i}{A_0} \quad (i = 1, 2, ..., 40). \tag{16}$$

Fig. 9 shows the relative amplitude distributions of the lowest 40 resonant modes in all of the numerical experiments. It is noted that in this figure, the symbol $f^* = f \Big/ \left(\sqrt{gh} \cdot D^{-1}\right)$ in the abscissa denotes the non-dimensional frequency, D denotes the length of the harbor shown in Fig. 4, and f_1^*=0.25 is the non-dimensional eigenfrequency of the 1st resonant mode of the harbor. From the figure, it is easily observed that the incident wave amplitude has dramatic influences on the relative wave energy distribution inside the harbor, which is reflected in the following two aspects. First, for all of the five groups, it can be seen that, when the incident wave amplitude is small, the wave energy inside the harbor is dominated by the lowest few resonant modes, and only a small proportion of the wave energy is distributed over the higher modes. However, with the increase of the incident wave amplitude, most of the wave energy inside the harbor is distributed over more resonant modes. In general, the relative energy distribution inside the harbor tends to become more uniform for the larger incident wave. Second, for the various types of the incident N-waves (Fig. 9a-d), as the incident wave amplitude increases, the resonant mode that possesses the highest wave energy shifts gradually from a lower mode to the higher mode. To better illustrate the phenomenon, Fig. 10 shows the variation of the resonant mode possessing the highest wave energy with respect to the incident wave amplitude in all of the numerical experiments. For the incident wave amplitude range studied in the paper, the resonant mode that possesses the highest wave energy in Groups A and B increases gradually from the 2nd mode to the 7th mode and to the

13th mode, respectively; in Groups C and D, the resonant mode shifts gradually from 1st mode to the 5th mode and to the 6th mode, respectively. However, significantly different from the N-wave, for the incident solitary waves, the highest wave energy inside the harbor is always possessed by the 1st resonant mode, which demonstrates that there exist obvious differences between the relative wave energy distributions induced by the N-waves and those induced by the solitary waves.

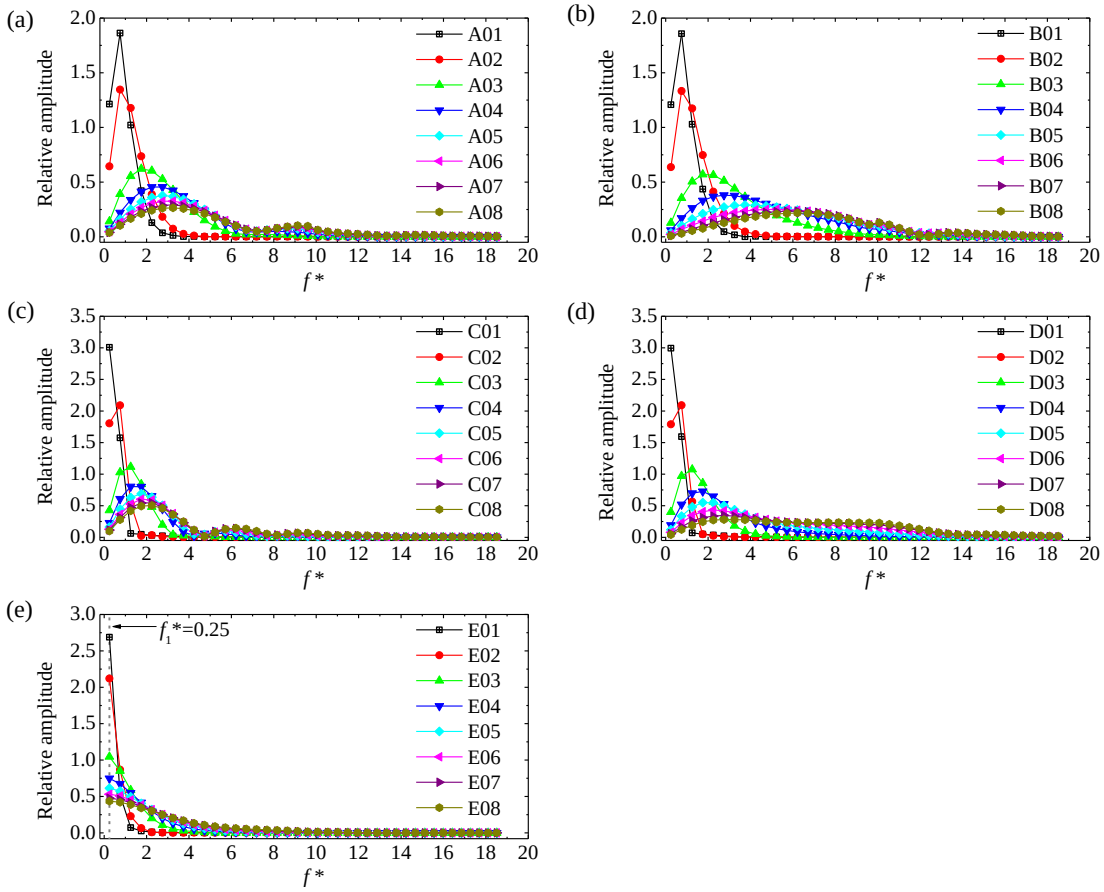

Fig. 9. Relative amplitude distributions of the lowest 40 resonant modes for all cases in (a) Group A, (b) Group B, (c) Group C, (d) Group D and (e) Group E, in which $f^* = f \Big/ \left(\sqrt{gh} \cdot D^{-1}\right)$ in the abscissa denotes the non-dimensional frequency, and D denotes the length of the harbor shown in Fig. 4. The vertical dashed line in (e) corresponds to the 1st resonant mode of the harbor, and its non-dimensional eigenfrequency is $f_1^*=0.25$.

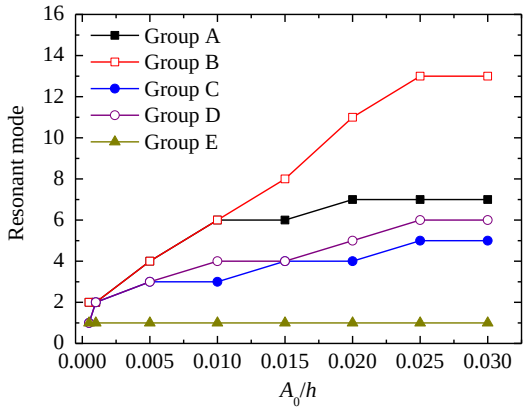

Fig. 10. The resonant modes with the highest wave energy for all cases

To qualitatively explain the phenomena shown in Figs. 9 and 10, the amplitude spectra of the various types of initial incident waves are demonstrated in Fig. 11. For the initial incident LEN and LDN waves of both the TS-type and the MS-type with the same amplitude, their waveforms are identical except that they are antiphase (refer to Eqs. (12) and (13)). Hence, their amplitude spectra are also identical with each other. From this figure, we can clearly see that for both the incident N-waves and solitary waves, when the incident wave amplitude is small, the incident wave energy is mainly concentrated in the low-frequency domain, and only a very small proportion of the wave energy is distributed over the higher frequency domain. As the incident wave amplitude increases, the proportion of the wave energy possessed by the higher frequency domain increases gradually, and the distribution of the incident wave energy over the frequency domain tends to become more uniform. This reasonably explains the phenomenon show in Fig. 9 that the relative energy distribution inside the harbor tends to become more uniform for the larger incident wave. From Fig. 11, it can also be clearly seen that for both the TS-type and the MS-type N-waves, the peak frequency of the incident waves shifts gradually from a lower frequency to the higher frequency; while for the incident solitary waves with different amplitudes, the peak frequency keeps unchanged and just equals to the 1st eigenfrequency of the harbor shown in Fig. 4. This well explains the phenomenon shown in Fig. 10 that for the N-waves, the resonant mode possessing the highest wave energy shifts gradually from a lower mode to higher one; while for the solitary waves, the highest wave energy inside the harbor is always possessed by the 1st resonant mode. It should be noted that for N-waves with large relative amplitude (A_0/h>0.001), their wave profiles during the propagation cannot keep the same as the initial waveform due to the

dispersive effect, and the larger relative amplitude leads to a faster and greater wave deformation [44]. Besides, for the LEN and LDN waves, their waveform evolutions during the propagation present different characteristics [45]. It leads to the other phenomenon shown in Fig. 10 that when the initial incident wave amplitude is relatively large, the resonant modes with the highest wave energy excited by the LEN and LDN waves of both the TS-type and the MS-type with the same amplitude are different, although their initial amplitude spectra are identical. More detailed discussions on the differences of the wave energy distributions inside the harbor induced by the LEN and LDN waves will be performed in Section 4.3.1.

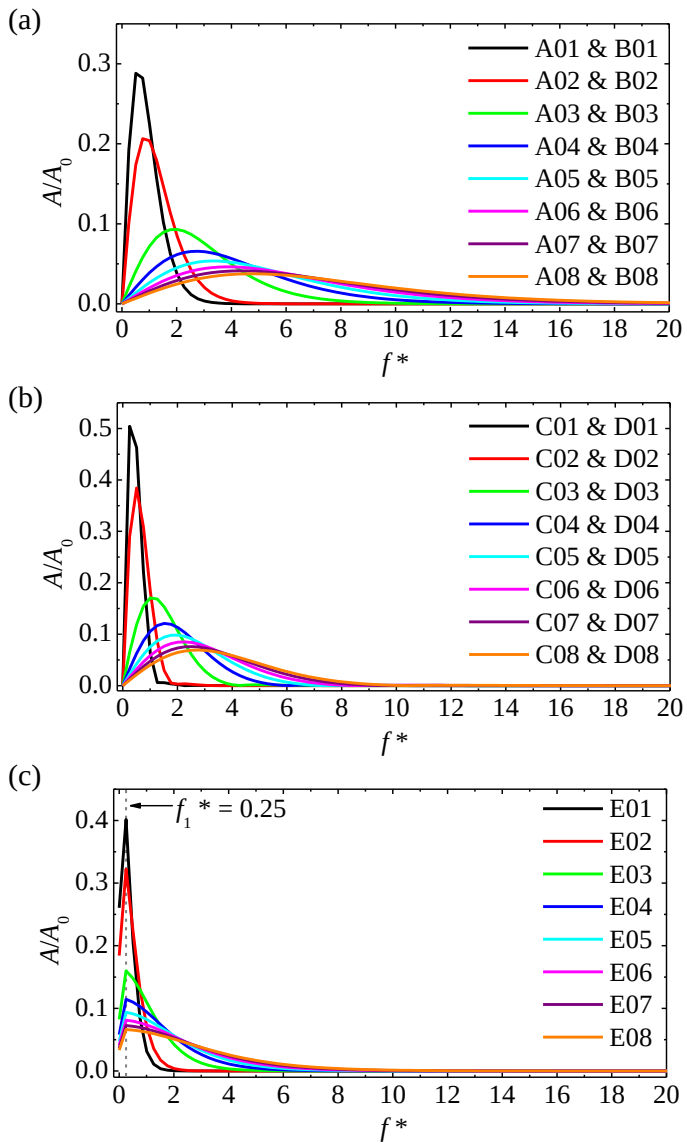

Fig. 11. Amplitude spectra of the various types of initial incident waves: (a) TS-type N-waves, (b) MS-type N-waves and (c) solitary waves. The vertical dashed line in (c) corresponds to the peak

frequency of the incident solitary waves, which equals the 1st eigenfrequency of the harbor shown in Fig. 4.

4.3. Effect of the incident wave type on the relative wave energy

In this section, the influence of the different types of the incident tsunami waves on the relative wave energy distribution inside the harbor is discussed in detail. Logically, the discussion can be analyzed from three different angles: (1) the effect of the N-wave and the solitary wave on the relative wave energy distribution; (2) for the TS- or MS type N-waves, the effect of the LEN wave and the LDN wave on the relative wave energy distribution; and (3) for the LEN or LDN waves, the effect of the TS-type N-wave and the MS-type N-wave on the relative wave energy distribution. For the first angle, it has been discussed in the Section 4.2 (refer to Fig. 10). Therefore, the effect of the incident wave type on the relative wave energy distribution is analyzed only from the last two angles in this section.

4.3.1. Effect of the LEN wave and the LDN wave

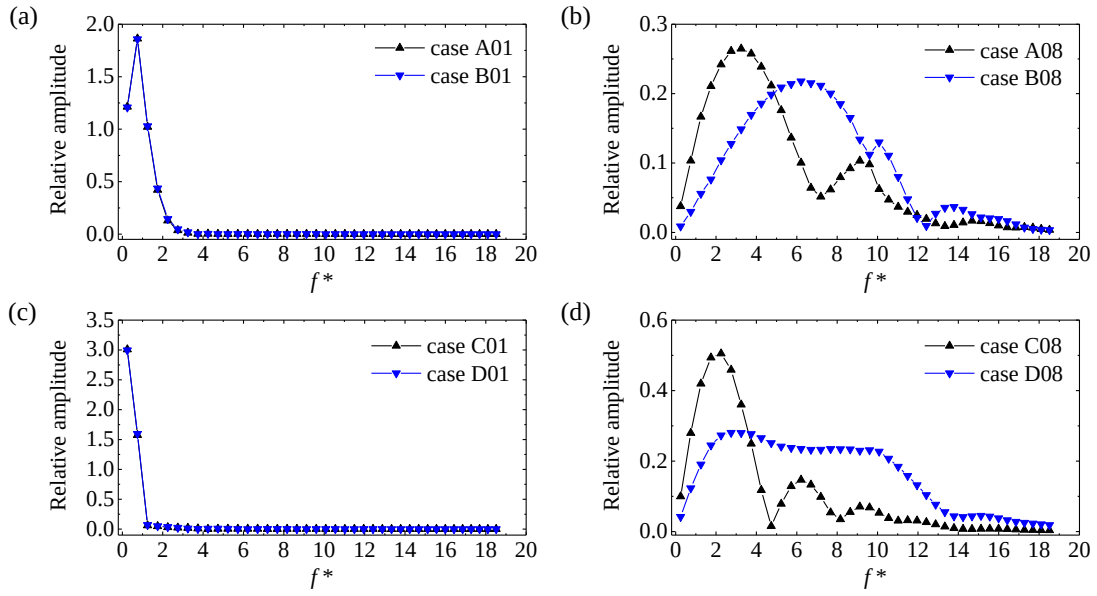

Fig. 12. Comparison of the relative amplitude distributions induced by the LEN wave and the LDN wave. (a) and (b) correspond to the TS-type incident N-wave with A_0=0.005 m and 0.30 m, respectively; (c) and (d) correspond to the MS-type incident N-wave with A_0=0.005 m and 0.30 m, respectively.

To visually show differences and similarities of the transient oscillations induced by the LEN wave and the LDN wave, a comparison of the relative amplitude distributions for the incident waves that have the same amplitude but different types is shown in Fig. 12. For the TS-type N-waves, when the incident wave amplitude is small (A_0=0.005 m) (Fig. 12a), the relative amplitude distributions excited by the isosceles LEN and LDN waves are almost identical to each other. Most of the wave energy is concentrated in the lowest four modes, and the second mode possesses the highest wave energy. Then, the wave energy inside the harbor deceases monotonously and rapidly observing the resonant mode. However, as the incident wave amplitude increases to 0.30 m (Fig. 12b), there arise obvious differences between the relative amplitude distributions excited by the isosceles LEN and LDN waves. For case A08, the highest relative wave amplitude, 0.265, is possessed by the 7th mode; while for case B08, the resonant mode that possesses the highest relative wave amplitude shifts up to the 13th mode, and the magnitude of the highest relative wave amplitude becomes 0.217. In general, the relative wave energy distribution in the latter seems to be more uniform than that in the former. Moreover, for both the two cases, there exist two secondary peaks over the higher resonant modes in the relative amplitude distribution and these peaks do not appear in the relative amplitude distribution for cases A01 and B01. For the MS-type N-waves, when A_0=0.005 m (Fig. 12c), similar to the TS-type N-wave, the relative amplitude distributions excited by the isosceles LEN and LDN waves are also almost identical to each other. The lowest two modes occupy almost the whole wave energy inside the harbor. As the incident wave amplitude increases to 0.30 m (Fig. 12d), the proportion of the wave energy distributed over the higher modes increases significantly in both cases C08 and D08. In addition, the relative wave energy distribution in the latter is perceptibly more uniform than that in the former. These phenomena observed for the MS-type N-waves are overall in accordance with those for the TS-type ones.

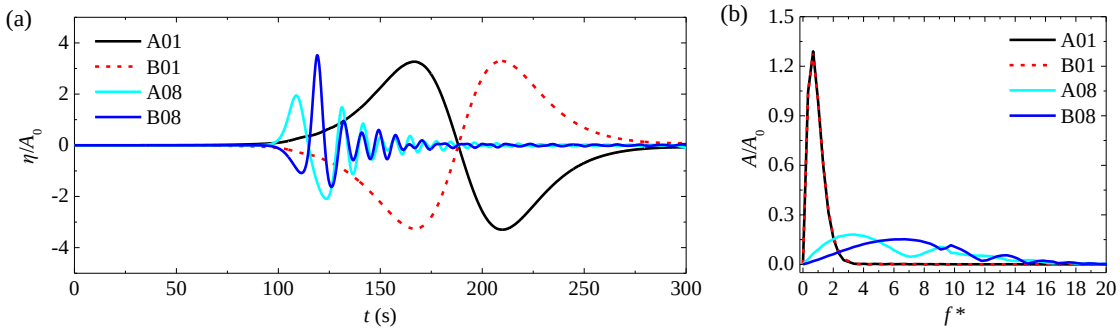

Fig. 13. Time series of the wave elevations at gauge G_{101} (a) and the corresponding amplitude spectra (b) for the TS-type incident N-waves with A_0=0.005 m and 0.30 m

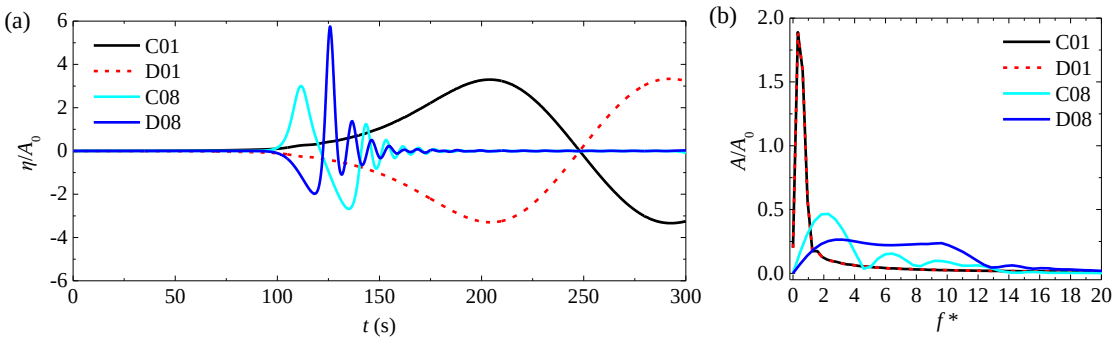

Fig. 14. Time series of the wave elevations at gauge G_{101} (a) and the corresponding amplitude spectra (b) for the MS-type incident N-waves with A_0=0.005 m and 0.30 m

To explain in detail the phenomena shown in Fig. 12, the time series of the wave elevations at gauge G_{101} and the corresponding amplitude spectra induced by the TS-type and the MS-type incident N-waves with A_0=0.005 m and 0.30 m are illustrated in Figs. 13 and 14, respectively. Take the TS-type incident N-waves (Fig. 13) for example. As pointed out by Zhao et al. [44] and Zhao [45], the wave profiles of the LEN and LDN waves with large relative amplitude (A_0/h>0.001) cannot keep the same as the initial waveforms during the propagation due to the dispersive effect, and their waveform evolutions present different characteristics. In cases A01 and B01, the relative amplitudes of the initial incident LEN and LDN waves are small ($A_0/h=5\times10^{-4}$). Therefore, their wave profiles will remain basically unchanged due to the negligible dispersive effect, which is reflected in the time series of the wave elevations at gauge G_{101} (Fig. 13a). Because the waveforms of the initial incident LEN and LDN waves are identical expect that they are antiphase, the time series of the wave elevations at gauge G_{101} are almost identical except that

they are antiphase; accordingly, their corresponding amplitude spectra are also almost identical with each other (Fig. 13b). In cases A08 and B08, the relative amplitudes of the initial incident LEN and LDN waves are large (A_0/h=0.03), and obvious wave deformations occur (Fig. 13a). In both the two cases, when the incident N-waves reach the backwall of the harbor, they finally evolve into a leading wave with N-wave characteristics followed by a dispersive wave tail. However, the time series of the wave elevations at gauge G_{101} in these two cases appear quite different characteristics, which are reflected in the following two aspects. First, the maximum runup of the LDN wave at the backwall of the harbor becomes significantly larger than that of the LEN wave. Due to strong dispersive effect, the maximum rundown of the LDN wave occurs when the second wave trough, rather than the first one, reaches the backwall, and its absolute value becomes less than that of the LEN wave (thorough discussions on differences of the maximum runup/rundown of various types of N-waves will be made in Section 4.5). Second, the period of the leading LDN wave becomes obviously less than that of the leading LEN wave, which is visually displayed in their amplitude spectra (Fig. 13b). Observing their amplitude spectra can easily find that the peak frequency for the LDN wave is significantly larger than that for the LEN wave, and the wave energy distribution over the frequency domain for the former seems to be more uniform than that for the latter, which are consistent with the related phenomena shown in Fig. 12b. For the MS-type incident N-waves, the phenomena illustrated in Fig. 14 are overall in agreement with those for the TS-type ones.

4.3.2. Effect of the TS-type and the MS-type N-wave

Fig. 15 compares the relative amplitude distributions for the incident waves that have the same amplitude but different types to intuitively demonstrate the differences and similarities of the transient oscillations excited by the TS-type and the MS-type N-waves. For the incident isosceles LEN wave, when the incident wave amplitude is small (A_0=0.005 m) (Fig. 15a), although in both cases A01 and C01, the majority of the wave energy is distributed over the lowest few modes, the relative wave energy distribution induced by the TS-type N-wave is more uniform than that by the MS-type one. Specifically speaking, most of the wave energy in case A01 is distributed over the lowest four modes; while in case C01, the lowest two modes possess almost all of the wave energy inside the harbor. When the incident wave amplitude increases to 0.30 m (Fig. 15b), the similar phenomenon as mentioned above can still be easily observed. In case A08, the majority of the

wave energy inside the harbor is distributed over the lowest fifteen modes; while in case C08, most of the wave energy is concentrated in the lowest nine modes. For the incident isosceles LDN wave, when A_0=0.005 m (Fig. 15c), the phenomenon is identical to that in Fig. 15a. However, when the incident wave amplitude increases to 0.30 m (Fig. 15d), the phenomenon is different from that in Fig. 15a-c. The wave energy distribution inside the harbor induced by the TS-type N-wave seems to be more concentrated than that by the MS-type N-wave, which will be further proved in Section 4.4.

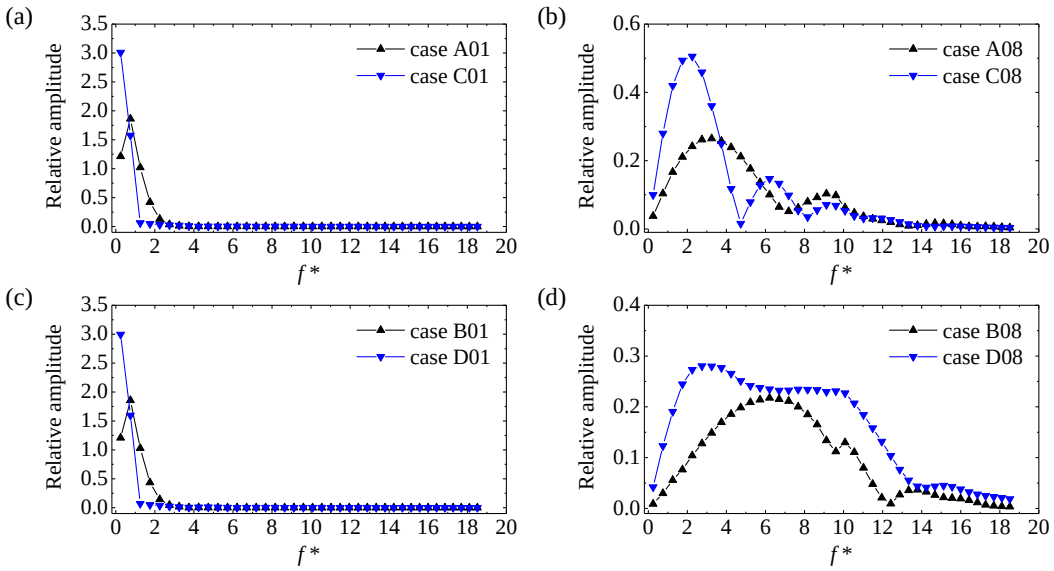

Fig. 15. Comparison of the relative amplitude distributions induced by the TS-type and the MS-type N-wave. (a) and (b) correspond to the incident LEN wave with A_0=0.005 m and 0.30 m, respectively; (c) and (d) correspond to the incident LDN wave with A_0=0.005 m and 0.30 m, respectively.

4.4. Quantification of the uniformity of the relative wave energy distribution

Because the significantly different characteristics of the relative wave distributions induced by N-waves and solitary waves, it is hard to directly (or qualitatively) compare their uniformity of the relative wave energy distribution inside the harbor. In addition, even only for N-waves, there also exists the same problem for some cases, such as cases B08 and D08 in Fig. 15d. Therefore, it is necessary to quantify the uniformity of the relative wave energy distribution induced by various types of tsunami waves. In this paper, the coefficients of variance of the relative amplitude distribution of the lowest 40 modes for all cases are calculated. The coefficient of variance (*CV*) is

589 defined as

590 $$CV = \frac{\sigma}{\mu}, \tag{17}$$

591 in which

592 $$\sigma = \sqrt{\frac{1}{40}\sum_{i=1}^{40}\left(\bar{A}_i - \mu\right)^2}, \tag{18}$$

593 $$\mu = \frac{1}{40}\sum_{i=1}^{40}\bar{A}_i . \tag{19}$$

594 It can intuitively reflect the discrete degree of the relative wave amplitude of different resonant
595 modes relative to their average value. Obviously, the smaller the coefficient of variance is, the
596 more uniform the wave energy distribution inside the harbor over different modes is.

597

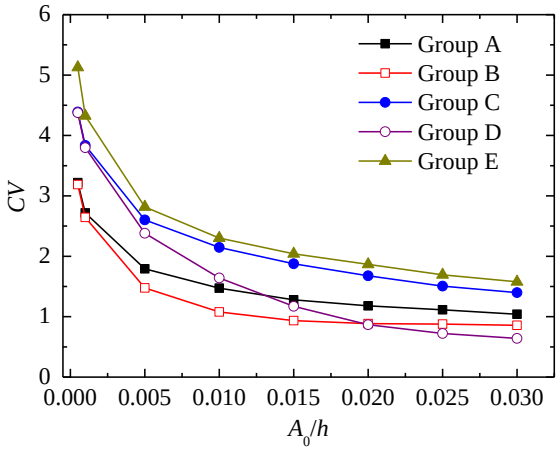

598

599 **Fig. 16.** The *CV* values of the relative amplitude distributions inside the harbor for all cases

600

601 Fig. 16 shows the *CV* values of the relative amplitude distributions inside the harbor for all
602 cases. Four obvious phenomena can be easily seen. First, for all of the five groups, the *CV* value
603 decreases monotonically with the increase of the incident wave amplitude, which is consistent
604 with the qualitative findings for Fig. 9. Second, the *CV* values in Group E are always larger than
605 those in Groups A-D, which illustrates that the relative wave energy distributions induced by
606 solitary waves are more concentrated than those induced by the various types of N-waves with the
607 same amplitude. Third, the *CV* values in Groups B and D are consistently less than those in
608 Groups A and C, respectively, when the incident wave amplitude is relatively large. This result
609 shows that, for both the TS-type and MS-type N-wave, the relative wave energy distributions
610 induced by the LDN waves are more uniform than those induced by the LEN waves when the

incident wave amplitude is relatively large, which agrees with the findings for Fig. 12. Fourth, the *CV* values in Group A are always lower than those in Group C, which demonstrates that, for the LEN waves, the relative wave energy distributions induced by the TS-type is always more even than those induced by the MS-type. However, for the LDN waves (Groups B and D), the result is different from the LEN waves. When the incident wave amplitude is small, the *CV* values in Group B are remarkably less than those in Group D; however, with the incident wave amplitude increases, the former gradually approaches and exceeds the latter. These quantitative results further prove the qualitative descriptions for Fig. 15.

4.5. Maximum runup and rundown inside the harbor

To investigate the relationship between the incident solitary wave amplitude and the maximum oscillation (runup) inside the harbor, Dong et al. [9], Gao et al. [11] and Gao et al. [14] carried out a series of numerical simulations and found that the maximum oscillation (runup) inside the harbor with flat or constant-slope bottom grows linearly with the incident solitary wave amplitude when the wave nonlinearity inside the harbor is relatively weak. In the current study, this discussion is extended to the maximum runup and rundown of the various types of N-waves inside the harbor.

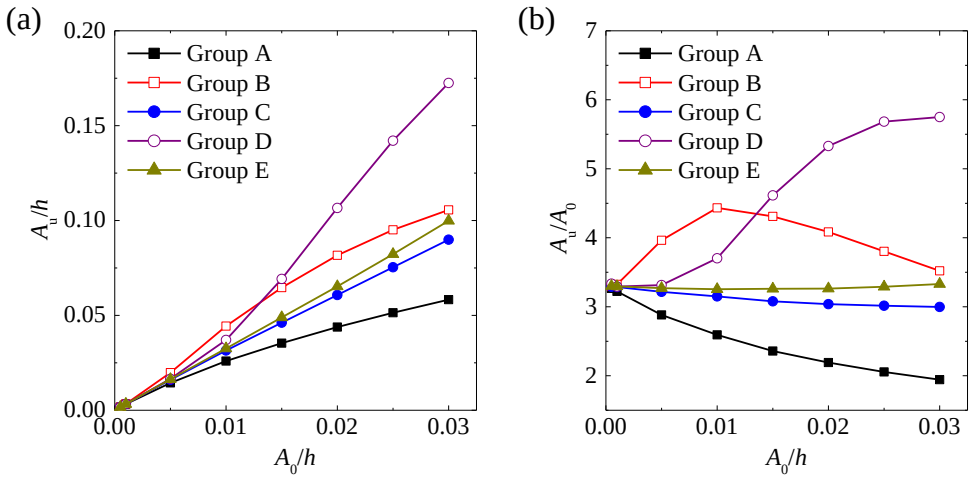

Fig. 17. Non-dimensional maximum runups, A_u/h, (a) and their amplification factors, A_u/A_0, (b) for all cases.

Fig. 17 shows the non-dimensional maximum runups, A_u/h, and their amplification factors, A_u/A_0, for all cases. The maximum runup of the various types of N-waves and their amplification

factors inside the harbor shows some different characteristics from those of the solitary waves. First, in term of the maximum runup (Fig. 17a), when the incident wave amplitude is small (A_0/h ≤0.001), all types of the incident waves considered in the paper have almost the identical maximum runup. However, with the increase of the incident wave amplitude, the maximum runups of both the TS-type and the MS-type LDN waves becomes gradually larger than those of the solitary waves; conversely, the maximum runups of both the TS-type and the MS-type LEN waves becomes gradually less than those of the solitary waves. When the relative wave amplitude A_0/h increases to 0.03, the MS-type LDN wave has the largest runup inside the harbor, which is significantly higher than those of the other four types of the incident waves. Therefore, from the viewpoint of tsunami-induced inundation, the LDN waves, especially the MS-type ones, are more likely to cause submersion near the port zone compared with the solitary waves and the LEN waves. Second, in terms of the amplification factor (Fig. 17b), as expected, the amplification factor for the solitary wave almost keeps constant in the incident wave amplitude range studied in this paper. The amplification factors for both the TS-type and the MS-type LEN waves decrease monotonically with respect to the incident wave amplitude. For the MS-type LDN waves, the amplification factor increases monotonically with the incident wave amplitude. For the TS-type LDN waves, their amplification factors increase first and then decrease with the incident wave amplitude. Similar to the maximum runup, the magnitude of the amplification factors for the solitary waves are less than those for both the TS-type and the MS-type LDN waves, and larger than those for both the TS-type and the MS-type LEN waves.

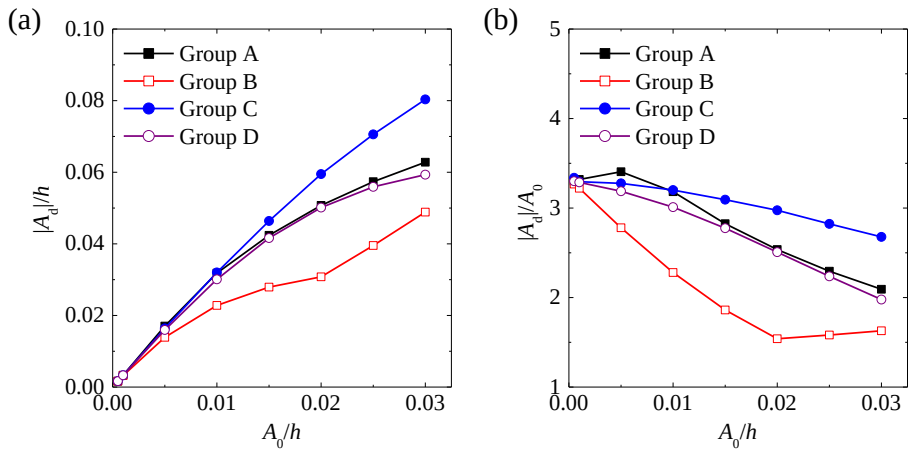

Fig. 18. Non-dimensional absolute values of the maximum rundowns, $|A_d|/h$, (a) and their

amplification factors, $|A_d|/A_0$, (b) for all cases.

Fig. 18 shows the non-dimensional absolute values of the maximum rundowns, $|A_d|/h$, and their amplification factors, $|A_d|/A_0$, for all of the numerical experiments. It can be seen that, when the incident wave amplitude is small ($A_0/h \leq 0.001$), all types of the N-waves considered in the paper have almost the identical maximum rundown. As the incident wave amplitude increases, the values of $|A_d|/h$ for the LEN become significantly larger than those for the LDN (Fig. 18a). Similarly, the amplification factor of the maximum rundowns, $|A_d|/A_0$, for the former also becomes considerably larger than the latter (Fig. 18b). Moreover, it can also be observed that, for both the MS-type LEN and LDN waves, the values of $|A_d|/A_0$ monotonically decrease with the incident wave amplitude. For both the TS-type LEN and LDN waves, the values of $|A_d|/A_0$ do not show a changing trend of monotonic increase or monotonic decrease.

5. Conclusions

Transient oscillations inside an elongated rectangular harbor induced by various types of incident N-waves, including the TS-type isosceles LEN and LDN waves and the MS-type isosceles LEN and LDN waves with different incident wave amplitudes, are first simulated using the FUNWAVE-TVD model. To show the similarities and differences between the oscillations excited by N-waves and those excited by solitary waves, the latter are also simulated in this paper, acting as a control group. Based on the numerical simulations and the NMD method [42, 43], this article focuses on the effects of the incident wave amplitude and the incident wave type on the relative wave energy distribution inside the harbor. The maximum runups and rundowns of the various types of the incident waves have also been studied. The results of this study will improve the understanding of transient harbor oscillations induced by tsunamis.

The following conclusions can be drawn from the results of the present study:

1. The relative wave energy distribution inside the harbor is greatly affected by the incident wave amplitude. For all types of tsunamis considered in this paper, when the incident wave amplitude is small, most of the wave energy is concentrated in the lowest few resonant modes. As the incident wave amplitude increases, the proportion of the wave energy distributed over the higher modes increases. Moreover, for the N-waves, the resonant mode possessing the highest wave energy shifts gradually from a lower mode to higher one. In conclusion, the

incident tsunami with a larger amplitude leads to more uniform relative wave energy distribution inside the harbor.

2. The type of the incident tsunami also has dramatic influences on the relative wave energy distribution inside the harbor, and they are reflected in the following three aspects. First, compared with the solitary wave, the N-wave with the same amplitude always induces the transient oscillation with a more uniform wave energy distribution inside the harbor. Second, the relative wave energy distributions induced by the LDN waves are consistently more uniform than those induced by the LEN waves, which is particularly noticeable when the incident wave amplitude is relatively large. Third, for the LEN wave, the relative wave energy distributions induced by the TS-type are always more uniform than those induced by the MS-type.
3. The maximum runups and rundowns of the tsunamis are sensitive to the incident tsunami type, which are also reflected in three aspects. First, when the incident wave amplitude is relatively large (A_0/h >0.001), the maximum runup for the LDN wave is always larger than that for the solitary wave; while the latter is always larger than that for the LEN wave. Second, unlike solitary waves, the amplification factor of the maximum runup for the various types of N-waves cannot remain unchanged. Third, for the absolute values of the maximum rundowns and their amplification factor, when A_0/h >0.001, both the magnitudes of $|A_d|/h$ and $|A_d|/A_0$ for the LEN wave are considerably larger than those for the LDN wave.

Finally, we reaffirm here that these conclusions are only valid for the elongated harbor with constant depth and when the relative amplitude of the initial incident wave, A_0/h, is less than 0.03.

Acknowledgments

This work was financially supported by the National Natural Science Foundation of China (Grant nos. 51609108, 51309124 and 51679113), the Natural Science Foundation of the Jiangsu Higher Education Institutions of China (Grant no. 16KJB570004), the State Key Laboratory of Coastal and Offshore Engineering at Dalian University of Technology (Grant no. LP1602), the Jiangsu Key Laboratory of Coast Ocean Resources Development and Environment Security at Hohai University (Grant no. JSCE201508) and the Jiangsu Key Laboratory of Advanced Design and Manufacturing Technology for Ship at Jiangsu University of Science and Technology (Grant

no. CJ1504).

References

[1] S. Tadepalli, C.E. Synolakis. The run-up of N-waves on sloping beaches. Proceedings of the Royal Society London A: Mathematical, Physical & Engineering Sciences. 1994; 445: 99-112.

[2] P.A. Madsen, H.A. Schäffer. Analytical solutions for tsunami runup on a plane beach single waves, N-waves and transient waves. Journal of Fluid Mechanics. 2010; 645: 27-57.

[3] A.B. Rabinovich. Seiches and harbor oscillations. In: Kim Y, editor. Handbook of Coastal and Ocean Engineering. Singapore: World Scientific Publishing; 2009. p. 193-236.

[4] M.P.C. De Jong, J.A. Battjes. Low-frequency sea waves generated by atmospheric convection cells. Journal of Geophysical Research. 2004;109, C01011, doi:10.1029/2003JC001931.

[5] G. Dong, J. Gao, X. Ma, G. Wang, Y. Ma. Numerical study of low-frequency waves during harbor resonance. Ocean Engineering. 2013; 68: 38-46.

[6] A.L Fabrikant. Harbor oscillations generated by shear flow. Journal of Fluid Mechanics. 1995; 282: 203-217.

[7] J.L. Luick, J.B. Hinwood. Water levels in a dual-basin harbour in response to infragravity and edge waves. Progress in Oceanography. 2008; 77: 367-375.

[8] G. Dong, G. Wang, X. Ma, Y. Ma. Numerical study of transient nonlinear harbor resonance. Science China-Technological Sciences. 2010; 53: 558-565.

[9] G. Dong, G. Wang, X. Ma, Y. Ma. Harbor resonance induced by subaerial landslide-generated impact waves. Ocean Engineering. 2010; 37: 927-934.

[10] J. Gao, C. Ji, O. Gaidai, Y. Liu. Numerical study of infragravity waves amplification during harbor resonance. Ocean Engineering. 2016; 116: 90-100.

[11] J. Gao, X. Ma, G. Dong, G. Wang, Y. Ma. Numerical study of transient harbor resonance induced by solitary waves. Proceedings of the Institution of Mechanical Engineers, Part M: Journal of Engineering for the Maritime Environment. 2016; 230: 163–176.

[12] C.B. Pattiaratchi, E.M.S. Wijeratne. Tide gauge observations of 2004-2007 Indian Ocean tsunamis from Sri Lanka and Western Australia. Pure and Applied Geophysics. 2009; 166: 233-258.

747 [13] G. Diaz-Hernandez, F.J. Mendez, I.J. Losada, P. Camus, R. Medina. A nearshore long-term
748 infragravity wave analysis for open harbours. Coastal Engineering. 2015; 97: 78-90.
749 [14] J. Gao, C. Ji, Y. Liu, O. Gaidai, X. Ma, Z. Liu. Numerical study on transient harbor
750 oscillations induced by solitary waves. Ocean Engineering. 2016; 126: 467-480.
751 [15] M. López, G. Iglesias. Long wave effects on a vessel at berth. Applied Ocean Research. 2014;
752 47: 63-72.
753 [16] P. Kumar, H. Zhang, K.I. Kim, D.A. Yuen. Modeling wave and spectral characteristics of
754 moored ship motion in Pohang New Harbor under the resonance conditions. Ocean
755 Engineering. 2016; 119: 101-113.
756 [17] X. Zhao, B. Wang, H. Liu. Characteristics of tsunami motion and energy budget during runup
757 and rundown processes over a plane beach. Physics of Fluids. 2012; 24: 062107.
758 [18] V.A. Vanoni, J.H. Carr. Harbor surging. Proceedings of the 1st International Conference on
759 Coastal Engineering. Long Beach, 1950. p. 60-68.
760 [19] J. Miles, W. Munk. Harbor paradox. Journal of the Waterways and Harbors Division. 1961;
761 87: 111-132.
762 [20] J.J. Lee. Wave induced oscillations in harbors of arbitrary geometry. Journal of Fluid
763 Mechanics. 1971; 45: 375-394.
764 [21] C.C. Mei, Y. Agnon. Long-period oscillations in a harbour induced by incident short waves.
765 Journal of Fluid Mechanics. 1989; 208: 595-608.
766 [22] G. Wang, J. Zheng, Q. Liang, Y. Zheng. Analytical solutions for oscillations in a harbor with a
767 hyperbolic-cosine squared bottom. Ocean Engineering. 2014; 83: 16-23.
768 [23] P.D. Girolamo. An experiment on harbour resonance induced by incident regular waves and
769 irregular short waves. Coastal Engineering. 1996; 27: 47-66.
770 [24] M.Y. Chen, C.C. Mei, C.K. Chang. Low-frequency spectra in a harbour excited by short and
771 random incident waves. Journal of Fluid Mechanics. 2006; 563: 261-281.
772 [25] G. Wang, J. Zheng, Q. Liang, W. Zhang, C. Huang. Theoretical analysis of harbor resonance
773 in harbor with an exponential bottom profile. China Ocean Engineering. 2015; 29: 821-834.
774 [26] G. Wang, G. Dong, M. Perlin, X. Ma, Y. Ma. An analytic investigation of oscillations within a
775 harbor of constant slope. Ocean Engineering. 2011; 38: 479-486.
776 [27] I.J. Losada, J.M. Gonzalez-Ondina, G. Diaz-Hernandez, E.M. Gonzalez. Numerical modeling

777 of nonlinear resonance of semi-enclosed water bodies: Description and experimental
778 validation. Coastal Engineering. 2008; 55: 21-34.
779 [28] T.G. Lepelletier, F. Raichlen. Harbor oscillations induced by nonlinear transient long waves.
780 Journal of Waterway, Port, Coastal and Ocean Engineering. 1987; 113: 381-400.
781 [29] G. Wang, G. Dong, M. Perlin, X. Ma, Y. Ma. Numerical investigation of oscillations within a
782 harbor of constant slope induced by seafloor movements. Ocean Engineering. 2011; 38:
783 2151-2161.
784 [30] P.L.F. Liu, Y.S. Cho, M.J. Briggs, U. Kanoglu, C.E. Synolakis. Runup of solitary waves on a
785 circular island. Journal of Fluid Mechanics. 1995; 302: 259-285.
786 [31] F. Camfield, R. Street. Shoaling of solitary waves on small slopes. J Waterways and Harbours
787 Div. 1969; 95: 1-22.
788 [32] D.G. Goring. Tsunamis - the propagation of long waves onto a shelf. Ph.D. dissertation, W. M.
789 Keck Laboratory of Hydraulics and Water Resources, California Institute of Technology,
790 Pasadena, California; 1978.
791 [33] C.E. Synolakis. The runup of solitary waves. Journal of Fluid Mechanics. 1987; 185:
792 523-545.
793 [34] S.C. Hsiao, T.W. Hsu, T.C. Lin, Y.H. Chang. On the evolution and run-up of breaking solitary
794 waves on a mild sloping beach. Coastal Engineering. 2008; 55: 975-988.
795 [35] H.Y. Lo, Y.S. Park, P.L.F. Liu. On the run-up and back-wash processes of single and double
796 solitary waves - An experimental study. Coastal Engineering. 2013; 80: 1-14.
797 [36] I. Charvet, I. Eames, T. Rossetto. New tsunami runup relationships based on long wave
798 experiments. Ocean Modelling. 2013; 69: 79-92.
799 [37] F. Shi, J.T. Kirby, J.C. Harris, J.D. Geiman, S.T. Grilli. A high-order adaptive time-stepping
800 TVD solver for Boussinesq modeling of breaking waves and coastal inundation. Ocean
801 Modelling. 2012; 43-44: 36-51.
802 [38] Q. Chen. Fully nonlinear Boussinesq-type equations for waves and currents over porous beds.
803 Journal of Engineering Mechanics. 2006; 132: 220-230.
804 [39] A.B. Kennedy, J.T. Kirby, Q. Chen, R.A. Dalrymple. Boussinesq-type equations with
805 improved nonlinear performance. Wave Motion 2001; 33: 225-243.
806 [40] G. Ma, F. Shi, J.T. Kirby. Shock-capturing non-hydrostatic model for fully dispersive surface

wave processes. Ocean Modelling. 2012; 43-44: 22–35.

[41] J.T. Kirby, W. Long, F. Shi. Funwave 2.0 Fully Nonlinear Boussinesq Wave Model On Curvilinear Coordinates. Newark: Center for Applied Coastal Research, Dept. of Civil & Environmental Engineering, University of Delaware; 2003.

[42] R.J. Sobey. Normal mode decomposition for identification of storm tide and tsunami hazard. Coastal Engineering. 2006; 53: 289-301.

[43] J. Gao, X. Ma, G. Dong, G. Wang, Y. Ma. Improvements on the normal mode decomposition method used in harbor resonance. Proceedings of the Institution of Mechanical Engineers, Part M: Journal of Engineering for the Maritime Environment. 2015; 229: 397-410.

[44] X. Zhao, B. Wang, H. Liu. Propagation and runup of tsunami waves with Boussinesq model. Proceedings of the 32nd International Conference on Coastal Engineering (ICCE) Shanghai, China, 2010.

[45] X. Zhao. Numerical Simulation of Generation, Propagation and Runup of Tsunamis. Shanghai: Ph.D Dissertation, Shanghai Jiao Tong University; 2011 (in Chinese).